Centrality dependence of isospin effect signatures in ^{124}Sn+^{64}Ni and ^{112}Sn+^{58}Ni reactions

R. Płaneta,[7,*] F. Amorini,[2,3] A. Anzalone,[2] L. Auditore,[4] V. Baran,[5] A. Benisz,[6] I. Berceanu,[5] A. Bonasera,[2] B. Borderie,[8] J. Borgensztajn,[22] R. Bougault,[9] M. Bruno,[10] J. Brzychczyk,[7] G. Cardella,[1] S. Cavallaro,[2,3] M. B. Chatterjee,[11] A. Chbihi,[12] M. Colonna,[2] M. D'Agostino,[10] R. Dayras,[13] E. De Filippo,[1] M. Di Toro,[2,3] J. Frankland,[12] E. Galichet,[8] W. Gawlikowicz,[19] E. Geraci,[10] G. Giuliani,[1,3] F. Giustolisi,[2,3] A. Grzeszczuk,[6] P. Guazzoni,[14] D. Guinet,[15] S. Kowalski,[6] M. Krauze,[6] E. La Guidara,[1,3] G. Lanzano,[1] G. Lanzalone,[2,3] N. Le Neindre,[8] J. Łukasik,[21] C. Maiolino,[2] Z. Majka,[7] N. G. Nicolis,[20] A. Pagano,[1] M. Papa,[1] M. Petrovici,[5] E. Piasecki,[18,19] S. Pirrone,[1] G. Politi,[1] A. Pop,[5] F. Porto,[2] M. F. Rivet,[8] E. Rosato,[17] F. Rizzo,[2] P. Russotto,[2] K. Schmidt,[6] K. Siwek-Wilczyńska,[16] I. Skwira-Chalot,[16] A. Sochocka,[7] L. Świderski,[18] A. Trifiro,[4] M. Trimarchi,[4] G. Vannini,[10] M. Vigilanti,[17] J. P. Wieleczko,[12] J. Wilczyński,[18] L. Zetta,[14] and W. Zipper[6]

(ISOSPIN Collaboration)

[1]*INFN, Sezione di Catania, Italy*
[2]*INFN, Laboratori Nazionali del Sud, Catania, Italy*
[3]*Dipartamento di Fisica e Astronomia, Universí di Catania, Italy*
[4]*INFN, Gruppo Collegato di Messina and Dipartamento di Fisica, Universí di Messina, Italy*
[5]*Horia Hulubei National Institute of Physiscs and Nuclear Engineering, Bucharest, Romania*
[6]*Institute of Physics, University of Silesia, Katowice, Poland*
[7]*M. Smoluchowski Institute of Physics, Jagiellonian University, Kraków, Poland*
[8]*Institute de Physique Nucleaire, IN2P3-CNRS, Orsay, France*
[9]*LPC, ENSI Caen and Universite de Caen, France*
[10]*INFN, Sezione di Bologna and Dipartimento di Fisica, Universí di Bologna, Italy*
[11]*Saha Institute of Nuclear Physics, Kolkata, India*
[12]*GANIL, CEA, IN2P3-CNRS, Caen, France*
[13]*DAPNIA/SPhN, CEA-Saclay, France*
[14]*INFN, Sezione di Milano and Dipartimento di Fisica, Universí di Milano, Italy*
[15]*IPN, IN2P3-CNRS and Universite Claude Bernard, Lyon, France*
[16]*Institute for Experimental Physics, Warsaw University, Warsaw, Poland*
[17]*INFN, Sezione Napoli and Dipartimento di Fisica, Universí di Napoli, Italy*
[18]*A. Sołtan Institute for Nuclear Studies, Świerk/Warsaw, Poland*
[19]*Heavy-Ion Laboratory, Warsaw University, Warsaw, Poland*
[20]*Department of Physics, University of Ioannina, Ioannina, Greece*
[21]*H. Niewodniczański Institute of Nuclear Physics, Kraków, Poland*
[22]*Institute of Physics, University of Zielona Góra, Zielona Góra, Poland*

Signatures of isospin effects were investigated for neutron-rich (^{124}Sn+^{64}Ni) and neutron-poor (^{112}Sn+^{58}Ni) systems at 35 MeV/nucleon for noncentral collisions. The centrality dependence of these signatures was tested for several impact parameter estimators. Our main observations are (i) the yields of ^{1}H and ^{3}He particles in the neutron-poor system are strongly enhanced with respect to the neutron-rich system, and the yields of ^{3}H, ^{6}He, and ^{7,8}Li are suppressed at all impact parameters, (ii) the yields of ^{2}H, ^{4}He, and ^{6}Li particles are almost the same for both systems, (iii) the N/Z ratio of intermediate mass fragments is correlated with the neutron richness of the system and is weakly dependent on the centrality of the collision, and (iv) the neutron richness of the detected fragments increases strongly with decreasing rapidity in the range from that of the projectile-like fragment to the c.m. region. The gross features of experimental data are reproduced by quantum molecular dynamics model calculations. A comparison between model calculations and the data indicates that the fragments produced in the c.m. regions are weakly excited.

I. INTRODUCTION

The isospin dependence of the nuclear equation of state (NEOS), is among the most important but poorly known properties of nuclear matter [1–3]. The knowledge of the density dependence of the symmetry energy term in NEOS

strongly influence (i) nuclear structure studies [4,5], e.g., the stability boundaries of neutron-rich nuclei and determination of neutron skin, (ii) nuclear reaction models, and (iii) the mechanism of nuclear multifragmentation. The interest in the properties of neutron-rich matter has also an astrophysical aspect, e.g., the mechanism of type II supernova explosions and the formation and structure of neutron stars.

Several approaches have been proposed to obtain information on the symmetry energy term $E_{\mathrm{sym}}(\rho)$ of the NEOS. For

*Corresponding author: ufplanet@if.uj.edu.pl

the case of low densities of nuclear matter, they include (i) the n/p ratio of fast preequilibrium nucleons [6], (ii) ^{3}H/^{3}He ratios, (iii) isospin diffusion [7–9], (iv) isospin distillation and isoscaling in nuclear multifragmentation [10], (v) neutron-proton differential flow [11], and (vi) neutron-proton and proton-proton correlation functions at low relative momenta [12].

Simulations of reaction dynamics showed [13] that collisions of asymmetric nuclei (in N/Z) could provide important information on the symmetry energy term of the NEOS. It was shown that the main reaction mechanisms, from fusion to deep inelastic and fragmentation, appear quite sensitive to the density dependence of the symmetry energy term in the nuclear equation of state. The calculations of Baran *et al.* [3] show evidence of characteristic patterns of behavior of the N/Z ratios for the intermediate mass fragment (IMF) as a function of the reaction centrality. In peripheral binary collisions, the IMF will be emitted in a statistical way from the excited projectile-like fragment (PLF) and target-like fragment (TLF) sources close to the stability line. For semiperipheral ternary events, the neck-fragmentation mechanism will form more neutron-rich IMFs. For central collisions, the neutron distillation will take place, and the fragments will again be much more symmetric with respect to the N/Z ratio. The relevance of such behavior is related to the stiffness of the symmetry term at subnuclear densities.

In our investigations, we focus on semiperipheral collisions. The formation of the fragments in the region between interacting nuclei has already been studied for a number of systems (see, e.g., Refs. [14–19]). Recently, the theory and experimental surveys of phenomena related to neck dynamics were presented by Di Toro *et al.* [20]. The formation of clusters in a dilute asymmetric matter but in contact with the regions of the PLF and TLF almost at normal densities reveals different isotopic effects and gives one an opportunity to study the mechanism of fragment formation for systems with different neutron richness.

The present analysis is performed using the experimental data for ^{124}Sn+^{64}Ni and ^{112}Sn+^{58}Ni systems measured at 35 MeV/nucleon. For these systems, central collisions were previously studied by Geraci *et al.* [21]. The isoscaling analysis based on the ratios of the isotopic yields was performed. It was shown that the results are consistent with the effect of isospin distillation. For the same systems, the class of ternary events involving the PLF, TLF, and one IMF was also investigated. The information about the time sequence and time scale of the IMF formation process was extracted [22,23]. For this class of events also the isoscaling analysis was performed [24]. These results were compared with those obtained for central collisions, as investigated by Geraci *et al.*

In this work, the isospin effects observed for these two reactions are studied. The properties of the forward part of the CHIMERA detector (see Sec. II) that was used in these measurements (the REVERSE experiment) and the reverse kinematics of studied reactions make it possible to detect and resolve isotopically light fragments originating in most cases from a PLF or from an intermediate velocity source (IVS), for a wide range of noncentral collisions.

Section II gives short information on the REVERSE experiment. The codes used in the model calculations are introduced in Sec. III. The procedure applied for the events selection is presented in Sec. IV. The results are discussed in Sec. V, and the conclusions are presented in Sec. VI.

II. REVERSE EXPERIMENT AND DATA

The experiment was performed at the Laboratori Nazionali del Sud in Catania, Italy, using the forward part of the CHIMERA 4π multidetector array [25]. In this experimental setup, a total of 688 Si-CsI(Tl) detectors were used, covering the polar angle range between $1°$ and $30°$ with full azimuthal symmetry around the beam axis. Reverse kinematics of ^{124,112}Sn+^{64,58}Ni reactions at 35 MeV/nucleon allowed the use of this setup as a nearly 4π device.

To identify the reaction products, several identification methods were used [25,26]. The mass of the fragments stopped in the silicon detectors was extracted by using the time of flight technique (TOF). The ΔE-E technique was applied to identify the charge of particles that punch through the silicon detectors. Isotopic identification was achieved for fragments with charge up to 9 in the angular range $11.5°$–$30°$. The light charged particles (LCP) that lose only a small part of their energy in silicon and are stopped in CsI(Tl) detector were identified by applying the pulse shape discrimination method to the signals delivered by a 18 x 18 mm photodiode, optically coupled to the crystal.

Thanks to very good performance of the detectors, the identification of the atomic numbers up to $Z = 50$ was achieved with good resolution (i.e., better than one unit for $Z < 40$) in the full dynamical range of the experiment. For charged particles up to $A \approx 30$, the TOF technique was used for mass identification of particles stopping in the Si detector. Further details of particle identification and energy calibration can be found in Ref. [26].

During the REVERSE experiment, data were collected requiring charged-particle multiplicity, $M \geqslant 2$ or 3 (depending on the run), as a trigger. More extensive description of the experimental conditions can be found in Ref. [21].

III. MODEL CALCULATIONS

A. Quantum molecular dynamics approaches

To interpret our experimental results, the predictions of two microscopic models of nuclear reactions quantum molecular dynamics (QMD) [27,28] and constrained molecular dynamics (CoMD-II) [23,29], were used. The CHIMERA code [27] is based on a quantum molecular dynamics (QMD) approach [28] with features of quasiparticle dynamics [30]. In the CHIMERA code, the effective nuclear potential includes the Pauli momentum dependent term. The Pauli potential simulates the fermionic nature of nucleons; i.e., it introduces repulsion between nucleons of the same kind that are too close in phase space. The two-body effects are taken into account by a nucleon-nucleon (NN) scattering term, and we use the experimental energy- and isospin-dependent NN

cross section [31], σ_{NN}. If the final states after collision are already occupied, the collision is not allowed (Pauli blocking), and the two nucleons continue their motion in the effective potential. In the CoMD-II approach, the fermionic nature of many-body problem is simulated by constraining the nucleon equations of motion to fulfill the Pauli principle on phase space by means of multiscattering processes. On average, good ground state properties of nuclei are obtained by coupling the Pauli principle request with a cooling-warming procedure. This method allows one to obtain ground state configurations with a time stability of several hundred fm/c. The values of the potential parameters correspond to a soft equation of state (EOS) ($K \approx 200$ MeV). Both models contain a density-dependent symmetry energy term. For the CHIMERA code calculations, the symmetry energy strength coefficient was parametrized as ASY-STIFF and ASY-SOFT according to the prescriptions of Ref. [32]. Additionally, to simulate in-medium effects, the NN cross section was parametrized as $(1 - 0.2\rho/\rho_0)\sigma_{NN}$. The calculations with this reduced nucleon-nucleon cross section were executed for the ASY-STIFF parametrization. In the CoMD-II calculations, the density dependence of the symmetry energy coefficient was described according to Ref. [29].

In the present analysis, an extensive comparison is made for the QMD model. For the CoMD-II model, the comparison is limited to observables related to fragment emission and is presented at the end of Sec. V.

B. CHIMERA code calculations

The calculations with the CHIMERA code were performed up to 300 fm/c; after that time, all nucleons separated in configuration space by less than 3 fm were assumed to form a cluster. For each cluster, the atomic number, mass number, position, momentum, spin, and binding energy were determined. The binding energy values were used afterward to calculate the excitation energies of hot fragments.

Figure 1 presents the QMD model predictions (before evaporation) for the case of noncentral collisions ($b = 6$–8 fm). The upper left panel shows the location of PLF, TLF, and IVS sources in the plane defined by parallel velocities of the fragments in the laboratory reference frame and their charges. The PLF source is located at velocities close to the beam velocity and a charge around the projectile charge. The TLF fragments are observed with small velocities and charges around 20. The fragments belonging to the IVS source are much smaller, and their parallel velocities distribution is very broad, centered at a velocity corresponding approximately to the nucleon-nucleon c.m. reference frame.

The upper right panel shows the location of the sources in the velocity space. We observe that the velocities of PLF and TLF fragments are well defined, whereas the velocities of IVS fragments are distributed in the region between PLF and TLF. The bottom left panel presents the charge distribution corresponding to the observed sources. The bottom right panel presents the asymmetry parameter for observed fragments as a function of their charge.
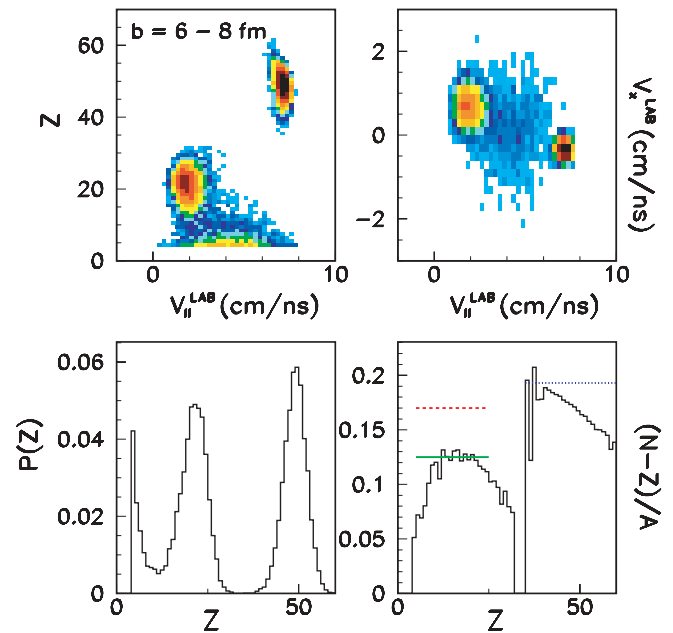

FIG. 1. (Color online) QMD model predictions for noncentral ($b = 6$–8 fm) collisions of ^{124}Sn+^{64}Ni reaction at 35 MeV/nucleon. Upper left panel: location of PLF, TLF, and IVS sources in the Z vs parallel (beam) velocity of the fragment plane; upper right panel: location of sources in the velocity space projected on the reaction plane (the impact parameter vector chosen to be in the x direction); bottom left panel: the charge distribution; bottom right panel: asymmetry parameter $I = (N - Z)/A$ of fragments as a function of their charge. Dotted blue, solid green, and dashed red lines correspond to the asymmetry parameter of projectile, target, and compound nucleus, respectively.

Information about the centrality dependence of isospin effects predicted by the model is given in Fig. 2. Here the average N/Z ratios of the *primary* TLF, *primary* PLF, and *primary* IVS fragments ($Z = 4$–8), for neutron-rich (upper red lines) and neutron-poor (lower blue lines) reactions, are shown. As can be seen, the N/Z ratio of PLF shows a weak tendency to decrease with decreasing impact parameter b for the neutron-rich reaction, while the opposite and less pronounced tendency is seen for the neutron-poor one. For the fragments created in the IVS source, the model predicts that their N/Z ratio for the neutron-rich system is larger than for the neutron-poor system. One observes an increase of the N/Z ratio moving from peripheral collisions to the midcentral collision, where the ratio reaches its maximum. One can also notice that for the IVS source, the N/Z ratio of the fragments is well below the ratios corresponding to the projectile, target, and compound nuclei. For the neutron-rich system, this observation is related to the fact that the emission of neutrons in the primary phase of the reaction is two times higher than the emission of protons. The model predictions for ASY-STIFF, ASY-SOFT, and ASY-STIFF+in-medium effects parametrizations are also shown. Notice that the differences in the N/Z ratios between model parametrizations are weak. This behavior is consistent with the fact that the maximum of nuclear matter in the initial phase of the reaction is predicted to be 30% higher than the density of the cold nucleus.
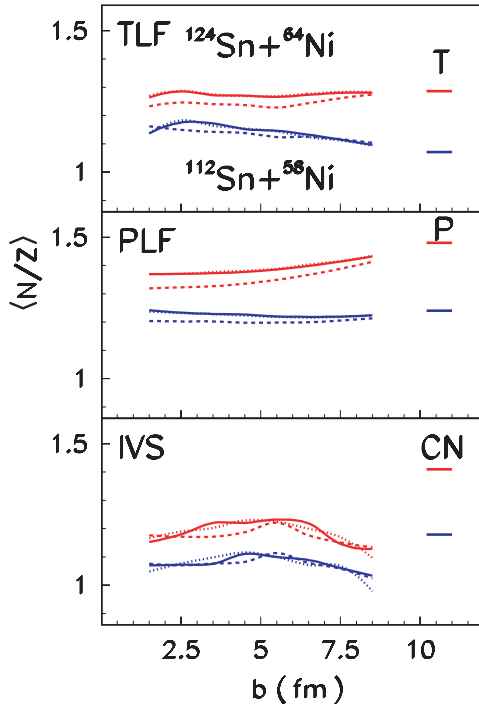
FIG. 2. (Color online) Results of QMD calculations for ^{124}Sn+^{64}Ni (upper red lines) and ^{112}Sn+^{58}Ni (lower blue lines) systems: average N/Z ratio of the primary TLF, PLF, and IVS fragments ($Z = 4$–8) as a function of impact parameter b for the ASY-STIFF (solid lines), ASY-SOFT (dashed lines), and ASY-STIFF (dotted lines) parametrizations and nucleon-nucleon cross-section reduced to $(1 - 0.2\rho/\rho_0)\sigma_{NN}$. Lines labeled T, P, and CN correspond to target, projectile, and compound nucleus N/Z ratios, respectively.

The hot fragments decay afterward via sequential decay which is simulated by the GEMINI code [33]. In the present calculations, the dynamical version of the GEMINI code was used. This version considers the time sequence of the excited fragment decay, using the appropriate decay time constants [34], and the equations of motion of all charged fragments moving in the mutual Coulomb field are integrated numerically. Such an approach presents an extension of the QMD in heavy-ion reactions. All simulation results were "filtered" by the software replica of the CHIMERA multidetector [35]. In the following sections, the comparison between the model predictions and experimental data is discussed.

We also assess the influence of the decay process of hot PLF, TLF, and IVS fragments on the observed isospin effects using the statistical model code MECO [36] in which the LCP and IMF emissions are treated consistently using the Hauser-Feshbach formalism. The results of the mentioned model calculations are discussed in the following sections.

IV. SELECTION OF NONCENTRAL COLLISIONS

In the Fermi energy range ($20 < E/A < 100$ MeV/ nucleon) of heavy-ion collisions, the reaction cross section is dominated by the contribution of dissipative binary reactions, which involves the formation of well-defined projectile- and target-like fragments [37], showing similarity with what is
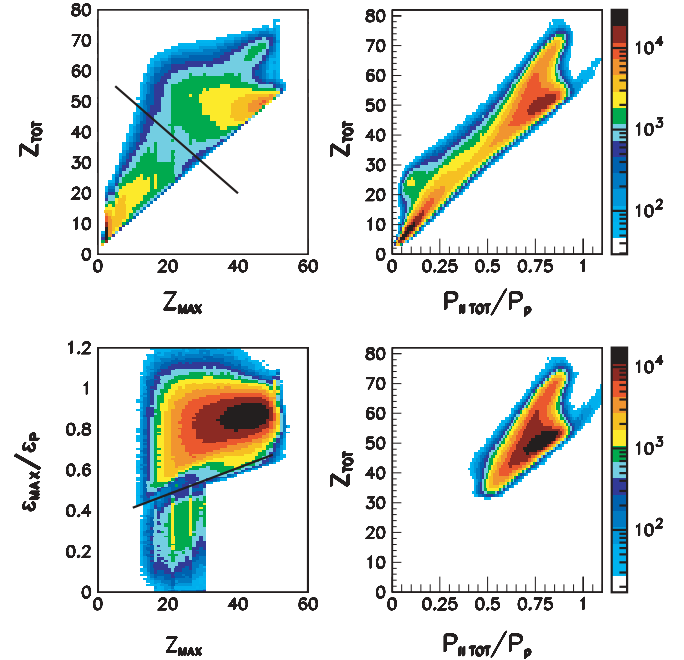

FIG. 3. (Color online) Left column: total charge $Z_{\rm TOT}$ vs heaviest fragment charge $Z_{\rm MAX}$ (top) and energy per nucleon $\varepsilon_{\rm MAX}$ of the heaviest fragment normalized to the projectile kinetic energy per nucleon ε_p vs. its charge $Z_{\rm MAX}$ (bottom). Right column: $Z_{\rm TOT}$ vs total parallel momentum normalized to the projectile momentum, $P_{\|{\rm TOT}}/P_p$ (top-no conditions, bottom-conditions described in the text).

observed at low bombarding energies (in, e.g., Ref. [38]). In the following, we focus our analysis on noncentral collisions (NCC), that is, collisions in which the PLF and the TLF are created. Such a definition covers a wide range of impact parameters and does not exclude the existence of an intermediate-velocity source [39–41] (see, e.g., Fig. 1).

The class of events corresponding to the NCC can be selected using different conditions placed on the experimental data. For example, one may use the correlation between the total detected charge, $Z_{\rm TOT}$, and the heaviest fragment charge, $Z_{\rm MAX}$. Such a selection is shown in the upper left panel of Fig. 3 for the ^{124}Sn+^{64}Ni system. Here we can distinguish two regions located above and below the solid line. The region below the line corresponds to very incomplete events, where $Z_{\rm TOT}$ represents a small fraction of the total charge of the system and the heaviest fragment has a charge well below the projectile charge. The region above the line is characterized by a large $Z_{\rm TOT}$ and detection of the PLF decay remnant.

With increasing excitation energy, the detected PLF charge ($Z_{\rm MAX}$) decreases. On the other hand, higher energy dissipation (excitation energy) is correlated with smaller kinetic energy of the PLF [37]. Such a correlation is presented for experimental data in the bottom left panel of Fig. 3 for the ^{124}Sn+^{64}Ni reaction. To elucidate the energy dissipation, the plot was made for the kinetic energy per nucleon for the heaviest fragment, $\varepsilon_{\rm MAX}$, divided by the projectile kinetic energy per nucleon, ε_P. The region below the thick solid line corresponds to events where the heaviest fragment is the TLF
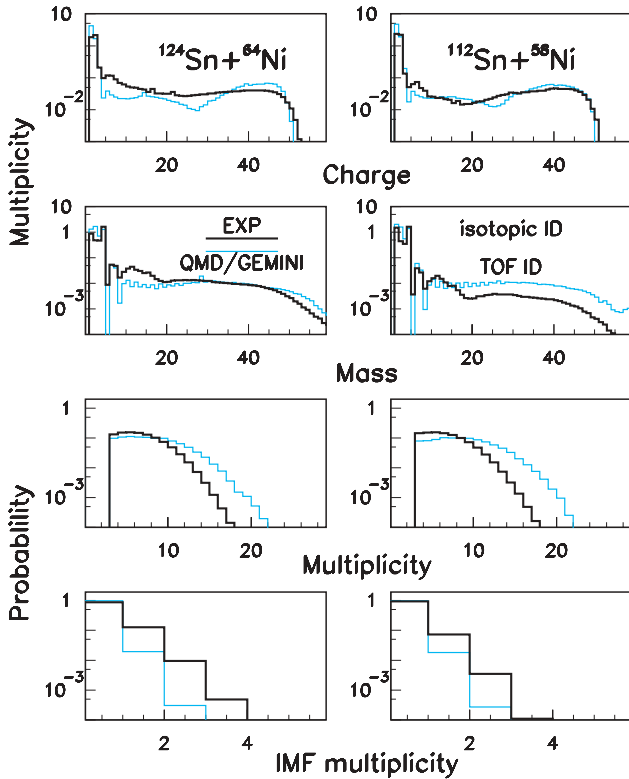
FIG. 4. (Color online) Charge spectra (top panels), mass spectra (isotopic and TOF mass identification), total and IMF ($Z_{IMF} = 4$–8) multiplicity distributions for the ^{124}Sn+^{64}Ni and ^{112}Sn+^{58}Ni systems. The IMF multiplicity is calculated for fragments visible with isotopic identification in the angular range of $11.5°$–$30°$. Black thick lines represent experimental data; blue thin lines, QMD/GEMINI calculations. The data and the model predictions are normalized to the respective number of events.

residue (the PLF remnant was not present) and is excluded from our analysis. Because of the very low thresholds, some of the TLF residues were detected in this experiment (note that TLF residues have much lower energy than PLF ones). The distinct correlation between the PLF energy per nucleon and the heaviest fragment charge (above the thick solid line) confirms that we have really selected the noncentral collisions with well-defined projectile-like and target-like fragments.

As a cross-check of our selection procedure, the dependence between the total detected charge, Z_{TOT}, and the total parallel momentum is presented in the right column of Fig. 3. The upper panel shows this dependence for all recorded events, and the bottom panel for events selected by the conditions set in the left column. In the following, the analysis of NCC collisions presented in this work is restricted to the class of well-defined events selected with the above-described conditions.

A comparison between the selected experimental data and the QMD/GEMINI predictions is shown in Fig. 4. Simulated reaction events were selected using the same conditions as in the case of the experimental data. As can be seen, the model overestimates the multiplicity of charged particles for both systems. However, the IMF multiplicities are underestimated in both systems. The same conclusions can be drawn from the
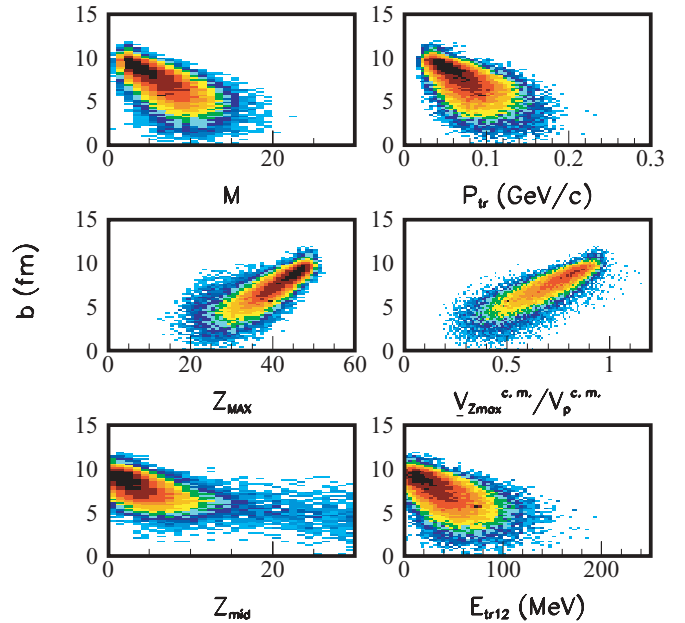

FIG. 5. (Color online) Impact parameter v selected estimators for ^{124}Sn+^{64}Ni reaction at 35 MeV/nucleon (QMD/GEMINI predictions).

comparisons between the experimental and calculated charge and mass distributions.

To study the NCC with respect to the centrality of the collision, it is necessary to use impact parameter related variables. Such variables allow us to analyze the reaction evolution with respect to excitation energy, energy dissipation, entrance channel angular momentum, etc. [42]. We tested several variables as impact parameter estimators for the class of the NCCs. Figure 5 shows a correlation between the impact parameter b and the multiplicity of charged particles M, the transverse momentum p_{tr}, the charge of the heaviest fragment Z_{MAX}, the velocity of the heaviest fragment in units of the projectile velocity in the c.m. system $V_{Z\,max}^{c.m.}/V_p^{c.m.}$, the charge collected in the midvelocity region Z_{mid}, and the transverse energy of light particles E_{tr12}. All these correlation plots were predicted by the QMD/GEMINI calculations for the NCCs. As one can see, the correlation is distinct for all tested impact parameter estimators with the only exception being the Z_{mid} variable.

Therefore, we performed our analyses by using the Z_{MAX}, E_{tr12}, and $V_{Z\,max}^{c.m.}/V_p^{c.m.}$ variables as impact parameter estimators. The observed reaction characteristics are very similar in these three sorting procedures. The results presented in this paper are relative to the $V_{Z\,max}^{c.m.}/V_p^{c.m.}$ estimator, with which the best sensitivity to the impact parameter is observed.

V. IMPACT PARAMETER DEPENDENCE OF ISOSPIN EFFECTS

Figure 6 presents the yield per event of different isotopes for $Z = 1, 2$, and 3 particles as a function of the $V_{Z\,max}^{c.m.}/V_p^{c.m.}$ impact parameter estimator for both studied systems. As one
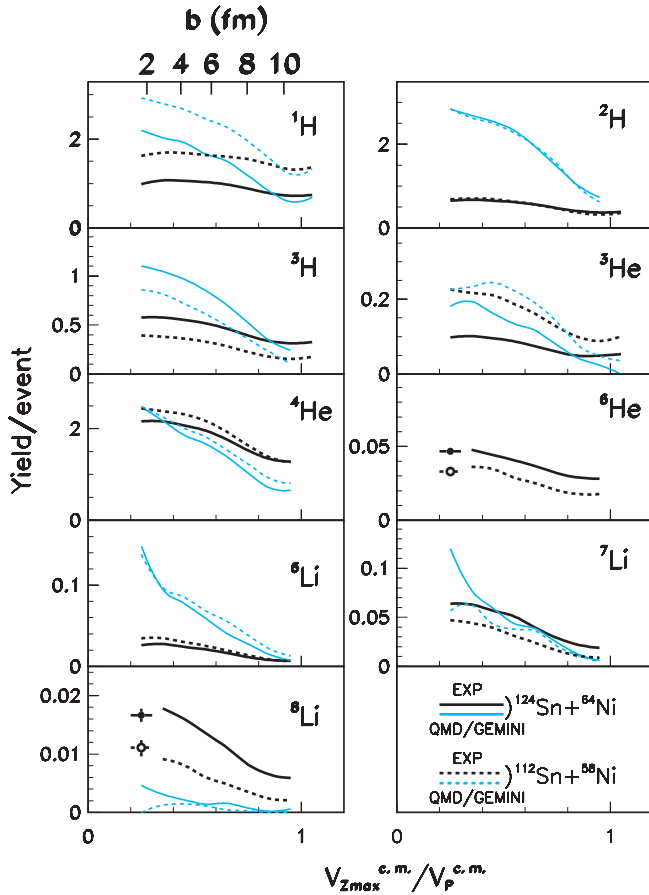
FIG. 6. (Color online) Yield per event of light particles and fragments as a function of velocity of the heaviest fragment normalized to the projectile velocity $V_{Z\,\mathrm{max}}^{\mathrm{c.m.}}/V_p^{\mathrm{c.m.}}$ for ^{124}Sn+^{64}Ni (thick solid lines) and ^{112}Sn+^{58}Ni (thick dashed lines) systems. In the cases of ^{3}H and ^{3}He, the energy thresholds typically of the order of 2–3 MeV/nucleon, as determined in the calibration procedure, were increased up to a value of 10 MeV/nucleon in order to avoid the contamination of more abundant ejectiles. For ^{6}He and ^{8}Li the statistical errors are quoted for the points marked by solid and open circles. Thin solid and dashed blue lines show the results of QMD/GEMINI calculations. Model predictions for ^{6}He are not quoted because of the very poor statistics obtained in the calculations.

can see, the multiplicity of the LCP emission increases with the centrality of the collision. One observes that the proton and ^{3}He yields are higher for the neutron-poor system than are the ^{3}H, ^{6}He, and ^{7,8}Li particles, which are emitted more abundantly from the neutron-rich system. Yields of particles with equal numbers of protons and neutrons, ^{2}H, ^{4}He, ^{6}Li, are practically identical for both investigated systems. One can also notice that the ratio of the yield of ^{3}H to the yield of ^{3}He particles is of the order of 5 for the neutron-rich system, whereas for the neutron-poor system this ratio is close to unity. However, these ratios depend somewhat on the applied energy threshold due to the different shapes of energy spectra for ^{3}H and ^{3}He ejectiles (see Fig. 6 caption).

The predictions of the QMD/GEMINI simulations are close to the experimentally observed yields for the most peripheral collisions (large $V_{Z\,\mathrm{max}}^{\mathrm{c.m.}}/V_p^{\mathrm{c.m.}}$). With an increase of collision
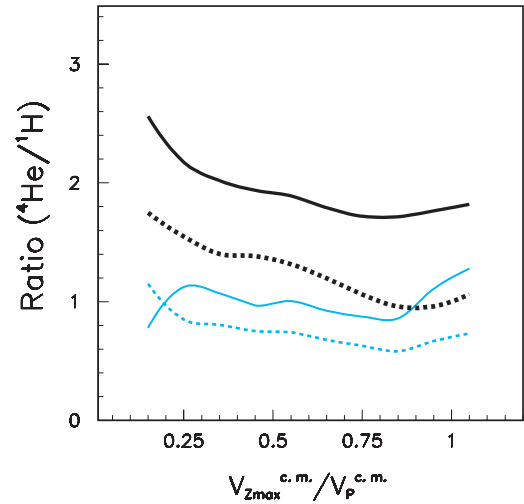
FIG. 7. (Color online) Ratio of α particle to proton yields per event as a function of $V_{Z\,\mathrm{max}}^{\mathrm{c.m.}}/V_p^{\mathrm{c.m.}}$ for ^{124}Sn+^{64}Ni (solid lines) and ^{112}Sn+^{58}Ni (dashed lines) systems. Experimental data are shown with thick black lines, and QMD/GEMINI calculations with thin blue lines.

centrality (decrease of $V_{Z\,\mathrm{max}}^{\mathrm{c.m.}}/V_p^{\mathrm{c.m.}}$), the model overestimates the emission rates, especially for hydrogen isotopes and ^{6}Li ions.

Figure 7 presents the ratio of the α particle to proton yield per event as a function of reaction centrality. One can see that the number of emitted α particles is larger than the number of emitted protons. This effect is more pronounced for the neutron-rich system and is more important for the more central collisions. These dependences might be partially due to the enhancement of cluster emission in the neutron-rich reaction. Since the "building" of clusters requires both neutrons and protons, more protons in the neutron-rich reaction are "used" for cluster emission than in the neutron-poor case. Consequently, in the neutron-rich system, the emission rate of protons decreases and the α emission rate increases. The model underestimates the observed ratio for both systems. The discrepancy between the model predictions and the data increases with the centrality of the collisions.

Besides light-particle analysis, the information about the dependence of the reaction mechanism on the isospin degrees of freedom is investigated by the isotopically resolved IMFs. The present analysis includes fragments with $Z = 4$–8 with isotopic identification in the angular range $11.5°$–$30°$. The average N/Z ratio of these IMFs is drawn in Fig. 8 as a function of $V_{Z\,\mathrm{max}}^{\mathrm{c.m.}}/V_p^{\mathrm{c.m.}}$. The N/Z ratios are presented for particles emitted by all sources and by PLF source, respectively. One observes that the average N/Z ratio is correlated with the neutron richness of the system. In the neutron-rich system, the observed ratio is, however, much smaller than the ratio corresponding to the composite system. This significant difference may be due to neutrons escaping the interaction region in a primary phase of the reaction. This behavior is not observed for the neutron-poor system. When no source selection is applied, a slight decrease of the average N/Z ratios with the centrality of the collision is observed for both reactions. This tendency is reversed for IMFs emitted in
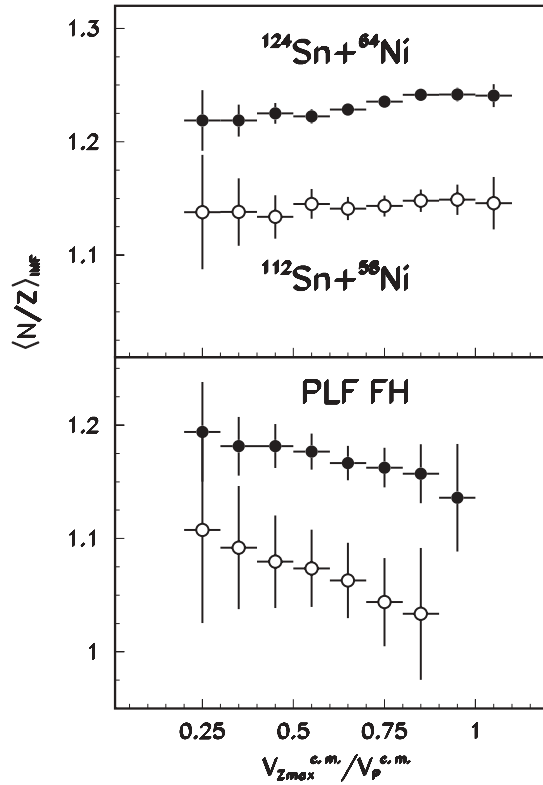
FIG. 8. Average N/Z ratio of IMFs ($Z_{\rm IMF} = 4$–8) visible with isotopic identification in the angular range of $11.5°$–$30°$ as a function of the heaviest fragment velocity normalized to the projectile velocity ($V_{Z\max}^{\rm c.m.}/V_p^{\rm c.m.}$), for ^{124}Sn$+^{64}$Ni (solid circles) and ^{112}Sn$+^{58}$Ni (open circles) systems. The upper panel presents the ratios for all observed particles, while the bottom panel presents the results for particles observed in the forward hemisphere of PLF source (PLF FH). Only experimental data are shown.

the forward hemisphere of the PLF source for both systems. Here for the peripheral collisions the forward hemisphere of the PLF source is well separated from the midrapidity source, and the observed fragments are emitted in a statistical way. For more central collisions, the contribution from the midrapidity source is significant even in the forward hemisphere of the PLF source, and the N/Z ratios in this case are much larger than in peripheral collisions.

More information about the IMF production can be obtained from the dependence of the average N/Z ratio of IMFs on the parallel velocity of the fragment in the laboratory system for both investigated reactions (upper left panel of Fig. 9). Here different curves correspond to different centrality regions selected by impact parameter estimator $V_{Z\max}^{\rm c.m.}/V_p^{\rm c.m.}$. One can observe a significant evolution of the N/Z ratio as a function of the parallel velocity. Fragments having velocities close to the c.m. velocity are more neutron rich than the fragments located in the PLF velocity region. One can also see that the curves corresponding to the neutron-rich system are located higher than those corresponding to the neutron-poor system. There is no significant dependence on the impact parameter estimator $V_{Z\max}^{\rm c.m.}/V_p^{\rm c.m.}$.

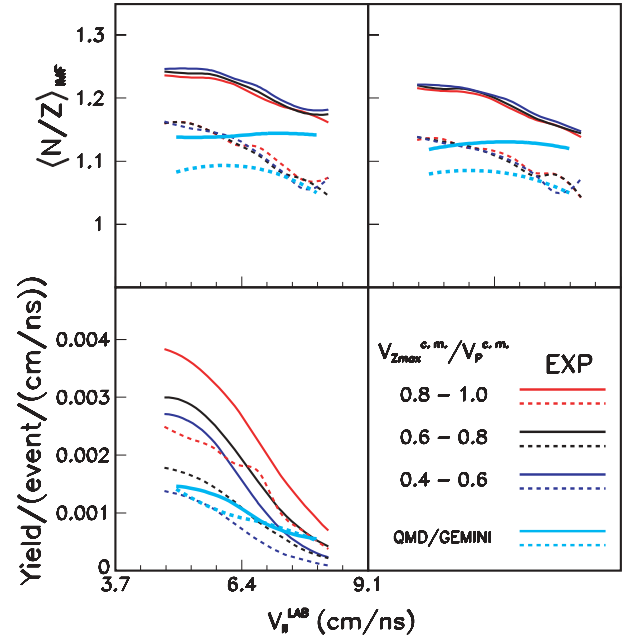FIG. 9. (Color online) Upper left: average N/Z ratios of IMFs ($Z = 4$–8) for the ^{124}Sn$+^{64}$Ni (solid lines) and ^{112}Sn$+^{58}$Ni (dashed lines) reactions as a function of parallel velocity of the fragment in the laboratory reference frame. The red, black, and blue lines correspond to different windows of $V_{Z\max}^{\rm c.m.}/V_p^{\rm c.m.}$ (experimental data). The light blue lines represent the N/Z ratio of secondary fragments $Z = 4$–8 originating from the decay of hot PLF, TLF, and IVS (QMD/GEMINI prediction); upper right: the corrected average N/Z ratio of IMFs under investigation; bottom left: the number of IMFs per event as a function of parallel velocity of the fragment.

Because the angular range of isotopically resolved fragments was limited, we made an attempt to correct the observed N/Z ratios. The upper right panel of Fig. 9 shows the N/Z ratios corrected for this limitation. For each bin of parallel velocity, the corrected value of N/Z ratio is given by

$$\langle N/Z \rangle_{\rm corr} = \frac{\sum_{Z_i=4}^{8} \langle N/Z \rangle_{Z_i} X_{Z_i}}{\sum_{Z_i=4}^{8} X_{Z_i}}, \tag{1}$$

where $\langle N/Z \rangle_{Z_i}$ is the mean ratio estimated for a given charge value, and X_{Z_i} is the number of Z_i fragments observed with charge identification in the full angular range of the apparatus. One observes that the corrected values of N/Z are somewhat smaller, and their dependence on the parallel velocity of the fragment is almost unchanged.

The lower left panel of Fig. 9 shows the number of observed IMFs per event as a function of parallel velocity of the fragment. One observes here that the number of fragments emitted in an event is larger for the neutron-rich system for all impact parameter windows. For both systems, the number of fragments decreases with the centrality of the collision.

The information about the isospin effects can be also extracted from the ratios of light fragments yields plotted as a function of parallel velocity of the fragment in the laboratory system (Fig. 10). One observes an important increase of neutron-rich isotope production (relative to neutron-poor isotopes) in the midrapidity region as compared with the PLF
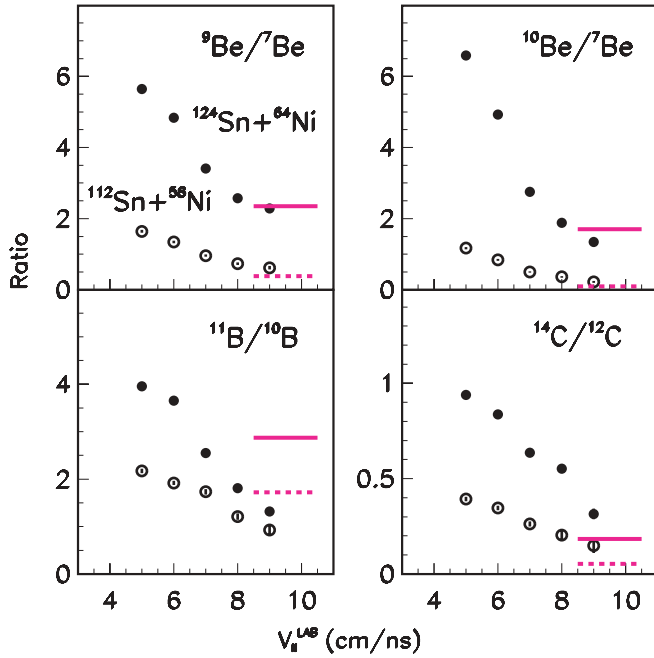
FIG. 10. (Color online) Ratios of isotope yields for Be, B, and C ions for ^{124}Sn$+^{64}$Ni (solid circles) and ^{112}Sn$+^{58}$Ni (open circles) systems as a function of parallel velocity of the fragment in the laboratory reference frame. The solid and dashed lines correspond to ratios calculated for evaporations from hot ^{119}In and ^{108}In nuclei using the statistical model code MECO.

FIG. 11. Upper panel: the average N/Z ratio of primary fragments belonging to the IVS source for the ^{124}Sn$+^{64}$Ni (solid squares) and ^{112}Sn$+^{58}$Ni (open square) reactions as a function of parallel velocity of the fragment in LAB reference frame (QMD model prediction); bottom panel: the N/Z ratio of secondary fragments ($Z = 4$–8) originating from the decay of hot PLF, TLF, and IVS (QMD/GEMINI prediction).

region. One can also notice that the ratios for the neutron-rich system are generally larger than those for the neutron-poor system. We checked that the ratios presented in this figure do not show any significant dependence on impact parameter estimators.

To understand the origin of fragments observed in the midrapidity region, we look more closely to the IVS source predicted by the QMD model (see Fig. 1). The upper panel of Fig. 11 shows the N/Z ratio for primary fragments belonging to the IVS source ($Z = 4$–8) predicted for neutron-rich and neutron-poor systems (solid and open squares).

The bottom panel presents the N/Z ratio for secondary fragments ($Z = 4$–8) originating from the decay of hot PLF, TLF, and IVS (solid and open squares). One observes a weak dependence on the parallel velocity of the detected fragment and on the system neutron richness. One can also notice that the N/Z ratio of these secondary fragments is much smaller than the N/Z ratio of primary IVS source.

The influence of the detection efficiency of the CHIMERA detector on the N/Z dependence shown in bottom panel of Fig. 11 is also tested. The upper left panel of Fig. 9 presents the results after applying the experimental limitations to the simulation (the solid and dashed light blue lines). One observes that the simulated average N/Z values after filtering are practically unchanged. One can also notice that the model predictions are in disagreement with experimental values in the c.m. region. The disagreement is also observed for the average masses of fragments. In the c.m. region, the masses
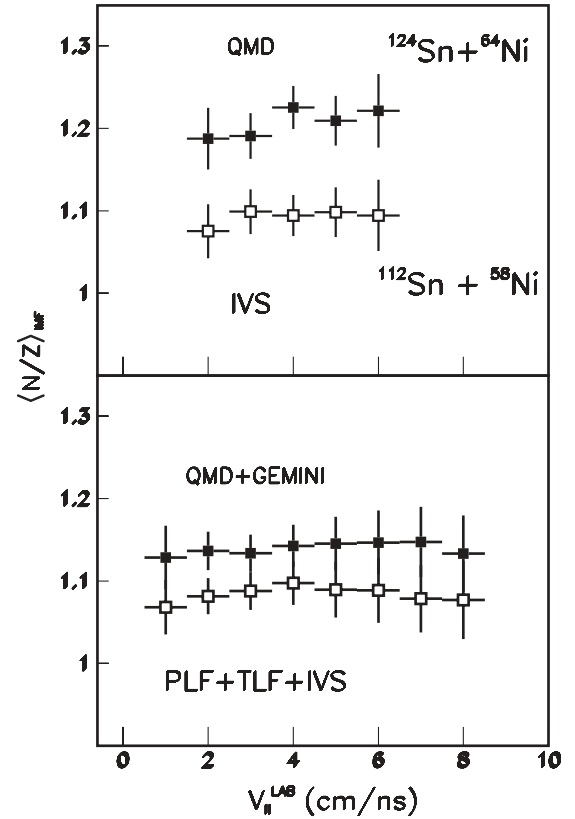
predicted by QMD/GEMINI calculations are smaller than the experimental ones.

For the PLF region, the experimental data presented in Fig. 10 are also compared with statistical model predictions using the MECO code. The ratios for individual isotopes are in agreement with the ratios calculated assuming the evaporation from hot ^{119}In and ^{108}In nuclei (solid and dashed straight lines in Fig. 10). These two hot nuclei correspond to the centroid of the PLF distribution predicted by the QMD model for noncentral collisions for both studied systems.

The disagreement between experimentally observed N/Z ratios and the QMD/GEMINI model predictions for the midrapidity region indicates that excitation energies of IVS fragments predicted by the QMD model are too high. Such a hypothesis is also supported by the statistical model predictions (MECO code) shown in Fig. 12. The upper panel shows the N/Z ratios of light fragments which might be produced in the IVS. The calculations were performed assuming 5 MeV/nucleon excitation energy (solid lines in middle and bottom panels), 3 MeV/nucleon (dashed lines), and 1 MeV/nucleon (dash-dotted lines). The highest value corresponds to the mean value of the excitation energy predicted by the QMD model for IVS fragments in noncentral collisions. Calculations at the lower
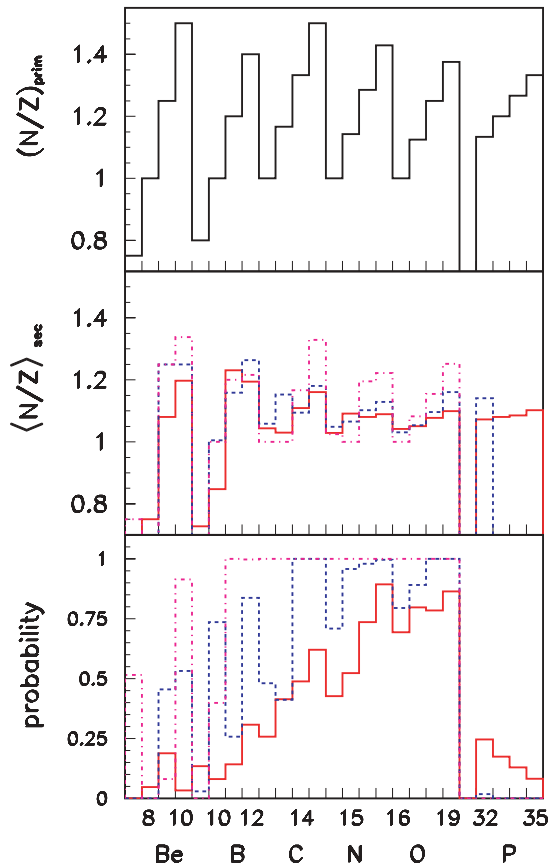
FIG. 12. (Color online) Statistical model predictions of the MECO code for evaporation from hot fragments which might be present in the IVS. The upper panel shows the N/Z ratios of these hot fragments (^{7,8,9,10}Be, ^{9,10,11,12}B, ^{12,13,14,15}C, ^{14,15,16,17}N, ^{16,17,18,19}O, and ^{32,33,34,35}P). The calculations were performed assuming that their excitation energy equals 5 MeV/nucleons (solid lines in middle and bottom panel), 3 MeV/nucleon (dashed lines), and 1 MeV/nucleon (dash-dotted lines). The middle panel presents the corresponding average N/Z ratios for distribution of emitted fragments ($Z = 4$–8) for each primary hot object. The bottom panel gives us the probability values that for a hot object we observe secondary fragments in the $Z = 4$–8 range. Calculations were performed for the spin of $3\hbar$.

energies test the assumption that the IVS fragments might be colder. The middle panel presents the corresponding average N/Z ratios of the emitted fragments of $Z = 4$–8 for each primary hot object. In these calculations the secondary decays from particle-unbound states were taken into account. The bottom panel shows the probability that for a given primary fragment we observe a secondary fragments with Z in the range of $Z = 4$–8.

The curves in the middle panel of Fig. 12 show that the evaporation process smears out the strong isospin effects observed for hot fragments. Calculations indicate that the secondary nucleon emission from particle unbound states is dominant in the smearing process. One observes that for primary nuclei, with an excitation energy of 5 MeV/nucleon, the average N/Z of secondary fragments exceeds 1.2 only in the case of ^{11}B nuclei. Making the assumption that the

excitation energy is equal to 3 MeV/nucleon, we observe that the corresponding N/Z values exceed 1.2 for ^{9,10}Be and ^{12}B fragments. For the lowest excitation energy, the average N/Z values are higher than 1.3 for ^{10}Be and ^{15}C ions. For fragments as heavy as P ions, the N/Z values are below 1.2, and the probability to produce secondary fragments with $Z = 4$–8 decreases with increasing mass of P ion.

Comparing experimental N/Z values of IVS fragments observed in the midvelocity region and the MECO code predictions, one can conclude that the fragments produced in the region between the projectile and the target are relatively small. Their excitations energies are smaller than those predicted by the QMD model.

This observation may indicate that the formation of neutron-rich fragments in the midvelocity region has a dynamical character, while the fragments in the PLF region are produced in an evaporation process. Similar observations were reported earlier (see, e.g., Ref. [16]).

An alternative description of the average N/Z for IVS fragments as a function of the laboratory velocity is given by the CoMD-II model. In this case, the dynamical calculations
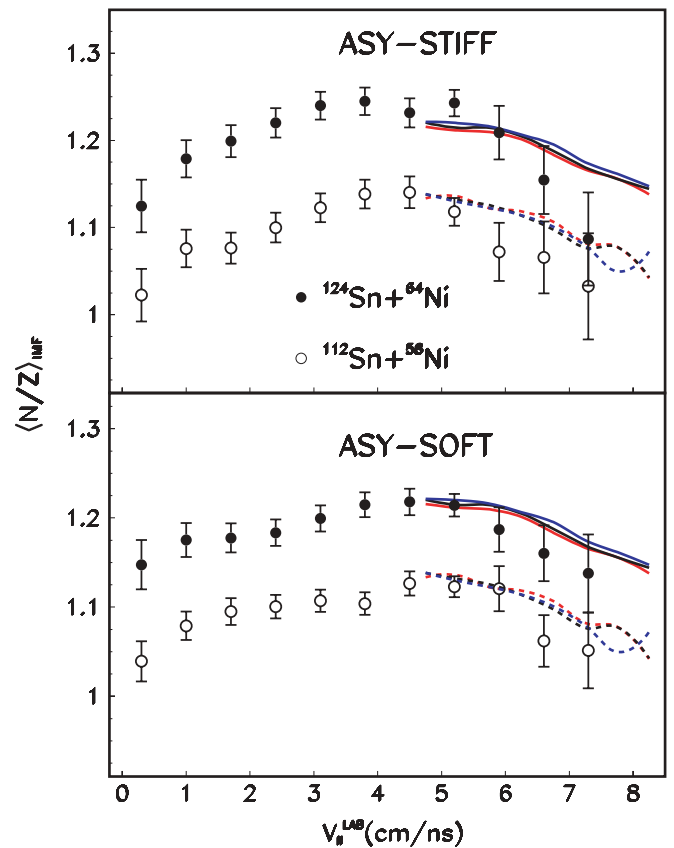

FIG. 13. (Color online) Corrected average N/Z ratios of IMFs ($Z = 4$–8) for ^{124}Sn+^{64}Ni (solid lines) and ^{112}Sn+^{58}Ni (dashed lines) reactions as a function of parallel velocity of the fragment in the laboratory reference frame (experimental data). Different curves correspond to different windows of $V_{Z\,max}^{c.m.}/V_p^{c.m.}$ (see Fig. 9). The average N/Z ratio of fragments generated by the CoMD-II model (solid and open circles) are presented for the ASY-STIFF (upper panel) and ASY-SOFT (bottom panel) parametrizations.

are performed up to 650 fm/c. At this time IMFs are basically cold. However, the PLF and TLF nuclei still have an average excitation energy of about 1.7–2 MeV/nucleon. Therefore, a second stage representing the cooling of the biggest fragments is applied to the primary events by using the GEMINI code. For the ASY-SOFT and ASY-STIFF parametrizations, the comparisons of the model predictions with experimental data are shown in Fig. 13. As one can see, the model reproduces relatively well the trends observed in experimental data even if the average N/Z calculated for velocities near the PLF region slightly underestimates the experimental value.

In particular, for the neutron-rich system, the different parametrizations produce, on average, fairly different slopes for laboratory velocities smaller or larger than the midrapidity velocity. The calculations show also that the slopes are correlated with the corresponding average IMF mass distribution. As an example, for the ^{124}Sn+^{64}Ni system, the average IMF mass values around 4.5 and 7 cm/ns are about 12.2 and 11 units, respectively; in comparison, the experimental values are about 12.8 and 12. A deeper investigation of the IMF production mechanism based on the CoMD-II calculations, which is beyond the scope of this article, is in progress.

VI. CONCLUSIONS

The centrality dependence of the isospin effect signatures for neutron-rich, ^{124}Sn+^{64}Ni, and neutron-poor, ^{112}Sn+^{58}Ni, systems were studied at 35 MeV/nucleon. Several impact parameter estimators were tested, and the centrality dependence of the observed isospin effects was found to be independent of the selection of a specific impact parameter estimator. For the class of light particles with $Z = 1, 2,$ and 3, one can observe that the yields of ^{1}H and ^{3}He particles in the neutron-poor system are enhanced with respect to the neutron-rich system, while the yields of ^{3}H, ^{6}He, and ^{7,8}Li show the opposite behavior for all impact parameters. One can also notice that yields of symmetric ^{2}H, ^{4}He, and ^{6}Li particles are independent of the neutron-richness of the system.

The N/Z ratio of the observed IMFs shows a correlation with the neutron richness of the systems under investigation.

However, in the case of the neutron-rich system, the observed N/Z ratio is much smaller than the ratio corresponding to the composite system. This significant difference may be due to neutrons escaping from the interaction region in the primary phase of the reaction. One can also notice a small decrease of the N/Z ratio with the centrality of the collision. This trend is reversed for fragments observed in the forward hemisphere of the PLF source indicating, a statistical evaporation from the PLF source for peripheral collisions.

In both reactions, the neutron richness of the observed fragments increases with the fragment's decreasing parallel velocity in the range from that of PLF region to the midrapidity region.

The QMD calculations, presented in this contribution, were performed with ASY-STIFF and ASY-SOFT parametrizations of the symmetry energy strength coefficient. For the ASY-STIFF parametrization, in-medium effects were also simulated. One observes a weak sensitivity for different parametrizations of the symmetry energy term in the nuclear equation of state [3] for both the primary (before evaporation) and secondary fragments. This conclusion might be related to the fact that the maximum compression of nuclear matter in the initial phase of the reaction is only 30% higher than the density of the cold nuclei.

The most significant disagreement between QMD/GEMINI predictions and experimental data is observed for the N/Z ratio for IMFs. This disagreement may indicate that excitation energies of the IVS fragments coming from the midrapidity region predicted by the QMD model are too high. Experimental data show that the production of neutron-rich fragments is much more probable than predicted by the model. This observation may be related to the fact that in the QMD model, the excessive neutrons are emitted in the initial phase of the reaction.

In the case of the CoMD-II model, the produced fragments are cold and the predicted average N/Z ratios are qualitatively in agreement with the experimental data. For the studied systems, deeper investigations are in progress, mainly devoted to a detailed description of the link between the rapidity dependence of the IMF's isotopic composition and the density dependence of the isospin forces.

[1] H. Müller and B. D. Serot, Phys. Rev. C **52**, 2072 (1995).

[2] Bao-An Li *et al.*, Nucl. Phys. **A699**, 493 (2002).

[3] V. Baran *et al.*, Nucl. Phys. **A703**, 603 (2002).

[4] B. A. Brown, Phys. Rev. Lett. **85**, 5296 (2000).

[5] C. J. Horowitz and J. Piekarewicz, Phys. Rev. Lett. **86**, 5647 (2001).

[6] W. U. Schröder and J. Tõke, Nucl. Phys. **A681**, 418c (2001).

[7] M. B. Tsang *et al.*, Phys. Rev. Lett. **92**, 062701 (2004).

[8] L. W. Chen, C. M. Ko, and B. A. Li, , Phys. Rev. Lett. **94**, 032701 (2005).

[9] V. Baran, M. Colonna, M. DiToro, M. Zielinska-Pfabe, and H. H. Wolter, Phys. Rev. C **72**, 064620 (2005).

[10] A. Ono, P. Danielewicz, W. A. Friedman, W. G. Lynch, and M. B. Tsang, Phys. Rev. C **68**, 051601(R) (2003).

[11] Bao-An Li, Phys. Rev. Lett. **85**, 4221 (2000).

[12] R. Ghetti *et al.*, Phys. Rev. C **69**, 031605(R) (2004).

[13] V. Baran *et al.*, Phys. Rep. **410**, 335 (2005).

[14] E. Plagnol *et al.*, Phys. Rev. C **61**, 014606 (1999).

[15] Y. Larochelle *et al.*, Phys. Rev. C **62**, 051602(R) (2000).

[16] P. M. Milazzo *et al.*, Nucl. Phys. **A703**, 466 (2002).

[17] S. Hudan *et al.*, Phys. Rev. C **70**, 031601(R) (2004).

[18] S. Hudan *et al.*, Phys. Rev. C **71**, 054604 (2005).

[19] S. Piantelli *et al.*, Phys. Rev. C **74**, 034609 (2006).

[20] M. Di Toro *et al.*, Eur. Phys. J. A **30**, 65 (2006).

[21] E. Geraci *et al.*, Nucl. Phys. **A732**, 173 (2004).

[22] E. De Filippo *et al.*, Phys. Rev. C **71**, 044602 (2005).

[23] M. Papa *et al.*, Phys. Rev. C **75**, 054616 (2007).

[24] E. De Filippo *et al.*, Acta Phys. Pol. B **37**, 199 (2006).

[25] A. Pagano *et al.*, Nucl. Phys. **A681**, 331 (2001) and references therein.

[26] M. Alderighi *et al.*, INFN-LNS Activity Report 2000, p. 59 (unpublished); J. Blicharska *et al.*, INFN-LNS Activity Report 2001, p. 113 (unpublished); N. Le Neindre *et al.*, Nucl. Instrum. Methods A **490**, 251 (2002); M. Alderighi *et al.*, *ibid.* **489**, 257 (2002).

[27] J. Łukasik and Z. Majka, Acta Phys. Pol. B **24**, 1959 (1993); J. Łukasik, private communication; J. Brzychczyk *et al.*, in Proceedings of the IWM2001, Catania, Italy (unpublished).

[28] J. Aichelin and H. Stöcker, Phys. Lett. **B176**, 14 (1986); J. Aichelin, Phys. Rep. **202**, 233 (1991).

[29] M. Papa, T. Maruyama, and A. Bonasera, Phys. Rev. C **64**, 024612 (2001); G. Giuliani and M. Papa, *ibid.* **73**, 031601(R) (2006).

[30] D. H. Boal and J. N. Glosli, Phys. Rev. C **38**, 1870 (1988); **38**, 2621 (1988).

[31] K. Chen *et al.*, Phys. Rev. **166**, 949 (1968).

[32] M. Colonna, M. DiToro, G. Fabbri, and S. Maccarone, Phys. Rev. C **57**, 1410 (1998).

[33] R. J. Charity *et al.*, Nucl. Phys. **A483**, 391 (1988).

[34] W. Gawlikowicz, Acta Phys. Pol. B **28**, 1687 (1997).

[35] W. Gawlikowicz, REPORT ZFGM-03-02, Kraków, 2003 (unpublished).

[36] N. G. Nicolis, private communication; A. Pakou *et al.*, Phys. Rev. C **71**, 064602 (2005).

[37] S. P. Baldwin *et al.*, Phys. Rev. Lett. **74**, 1299 (1995).

[38] W. U. Schroder and J. R. Huizenga, in *Treatise on Heavy-Ion Science* (Plenum Press, New York, 1984), Vol. 2, p. 113.

[39] L. Stuttgè *et al.*, Nucl. Phys. **A539**, 511 (1992).

[40] J. Tõke *et al.*, Nucl. Phys. **A583**, 519 (1995); Phys. Rev. Lett. **77**, 3514 (1996).

[41] L. G. Sobotka *et al.*, Phys. Rev. C **62**, 031603(R) (2000).

[42] J. D. Frankland *et al.*, Nucl. Phys. **A689**, 905 (2001).